

Research Article

Analysis of Human Thermal Comfort in Bus Based on Thermoelectric Cooling Climate-Controlled Seats

Chu-qi Su ^{1,2}, Xi-xian Liang ^{1,2}, Yi-ping Wang ^{1,2}, Ya-feng Yang ^{1,2}, Jian-jun Su,³
and Xun Liu ^{1,2}

¹Hubei Key Laboratory of Advanced Technology for Automotive Components, Wuhan University of Technology, 430070 Wuhan, China

²Hubei Collaborative Innovation Center for Automotive Components Technology, Wuhan University of Technology, 430070 Wuhan, China

³Hubei QiXing Vehicle-Body Co., Ltd., Suizhou, China

Correspondence should be addressed to Xun Liu; liuxun@whut.edu.cn

Received 3 October 2022; Revised 27 November 2022; Accepted 28 November 2022; Published 3 February 2023

Academic Editor: Geng Chen

Copyright © 2023 Chu-qi Su et al. This is an open access article distributed under the Creative Commons Attribution License, which permits unrestricted use, distribution, and reproduction in any medium, provided the original work is properly cited.

In order to improve the thermal comfort of passengers, the thermoelectric cooling climate-controlled seats were set in the passenger cabin. In this study, thermoelectric cooler units' cooling performance is studied by experiment method. The heat and flow field of the bus cabin are analyzed in four different cases (air conditioner open/closed, thermoelectric cooler open/closed) using computational fluid dynamics method. Moreover, an experiment has been conducted to verify the accuracy of the simulation method. The results show as below: the ideal working current of the thermoelectric cooler is in range of 3-4 A and the coefficient of performance value range 0.5-0.7. The climate-controlled seats can enhance the local airflow perturbation, which can increase the passengers' overall thermal comfort by 18.96%. The thermal comfort of passengers closer to air conditioner inlet is better than passengers in other areas, and the area with the best thermal comfort for passengers are the front and rear seats of the bus cabin. As expected, the thermoelectric cooling climate-controlled seat can improve the thermal comfort of passengers, and has a broad application prospect.

1. Introduction

The passengers' thermal comfort has become a major concern in the vehicle design. At present, the passenger's thermal comfort in the hot summer can be improved by adjusting the traditional air conditioner's (AC) air temperature, angle, and speed, however, the airflow cannot reach the back and buttocks of the passengers, which may contribute to heat and moisture accumulation [1]. Climate-controlled seats can increase the passengers' thermal comfort by blowing away the heat and moisture, which can establish a comfortable local thermal environment [2]. And the thermoelectric cooling (TEC) technology has the advantages of simple-design, lightweight, and environment-friendly, which leads to the increase application in engineering [3-5]. As a result, the thermoelec-

tric cooling climate-controlled seat can improve passengers' thermal comfort.

In recent years, experiments and numerical simulations have been conducted to prove the practicality of TEC application in many domains such as radiation cooling, medium temperature disinfection, and clothing drying [6-8]. By analyzing the relationship of the TEC's performance efficiency and working energy consumption, Yuan et al. [9] applied the TEC to the small-insulated vans and searched for the ideal working current. However, the current TEC coefficient of performance (COP) value is about 50% of the compression refrigeration method, and the TEC cannot work long hours in the condition of large temperature difference between indoor and outdoor. Zhang et al. [10] integrated TEC with a liquid cooling suit (LCG) to increase the thermal

comfort of the human body in high temperature environment, and they also evaluated the cooling performance under a specified cooling temperature. Although the temperature can be decreased by $6.6^{\circ}\text{C kg}^{-1}$ (defined specific temperature), which is a significant improvement compared with the previous garment, the weight of the TEC added to the wearer's load may result in some pain. Moreover, the LCG performs poorly in terms of ventilation, which makes it difficult for people to expel their sweat.

Many studies on the thermal comfort of automobile passengers have been conducted recently and the majority of them concentrated on the controlling and forecasting of the thermal environment of the vehicle's passenger compartment. The shoulders, back, sides, and buttocks of the human body are most sensitive to temperature in the seated position, according to Rosaria et al. [11] who employed an experiment to assess the temperature change of the zone between the person and the car seat. It provides theoretical guidance for designing cooling and heating system of intelligent seat. Through combining theory and experiment, Pala and Oz [12] compared the different effects of parameter changes on the thermal comfort of occupants, and established a general mathematical model and related experimental procedures. In order to simulate the dynamic thermal sensation of occupants under real driving conditions, Yun et al. [13] obtained equations for the overall thermal sensation (OTS) of female drivers under transient and steady-state conditions by long-term outdoor experiments. And there was a strong correlation between actual OTS and predicted OTS, which provides reliable reference equation for OTS prediction. In order to establish the dynamic thermal environment model of vehicles, Waley et al. [14] used the computational fluid dynamics (CFD) method and machine learning method to forecast the thermal comfort of vehicle passengers under different scenarios (window surface, ambient temperature, and outlet air temperature), and the error between the predicted value and the experimental value is less than 5%.

The local thermal environment of occupants should not be improved only by thermal environment prediction, but also by increasing human local thermal comfort. However, the effective strategy for increasing human thermal comfort has not been well studied. Su et al. [15] combined the climate-controlled seat with the thermoelectric cooler and used it in the cockpit of a commercial vehicle. They discovered that the average cab temperature decreased by 4°C in 60 seconds, and the passenger back temperature decreased from 33.5°C to 25.7°C . This shows that the thermoelectric climate-controlled seat enhances the thermal comfort of the occupants and reduce energy consumption, but the effect of temperature-controlled seats with multiple occupants was not considered. Hatoum et al. [16] incorporated a heat pipe into the seat and used it to absorb heat from the human body's back, increasing passenger thermal comfort by 30%. They also coupled a heat pipe model with a human biothermal model to forecast the back and overall thermal comfort. Afzal et al. [17] filled the gaps with a phase-change substance between the doors and roofs with coconut oil to control the temperature and relative humidity in the car cabin. Accord-

ing to the results, the temperature of the cabin drops by 13°C , and the relative humidity goes up by 8.6 percent.

In hot summer, high temperature outside the vehicle and high solar radiation could reduce cooling capacity of air conditioners, which will make the local thermal environment of the passengers worse. Many studies have used local air conditioners to improve the thermal comfort of passengers, but they have changed the original air conditioning structure of the car, or the research have neglected the discomfort caused by the sense of blowing. Therefore, the objective of this study is to determine the effect of the thermoelectric cooling climate-controlled seats on thermal comfort of passengers, analyze the optimal working condition of the TEC, and compare the thermal comfort of passengers in different seats. In other words, it is aimed at improving the passengers' local thermal comfort by thermoelectric climate-controlled seats without changing the original air conditioner system.

2. Analysis of Thermoelectric Temperature Control Seat Performance

2.1. The Principle of Thermoelectric Cooler. The thermoelectric device utilized in the climate-controlled seat operates on a concept based on the Peltier effect [18], which is different from the conventional compression refrigeration method. The temperature of one end of the P-N junction rises while the other end decreases as current flows through the P-N junction of the thermoelectric element. The thermoelectric element's heat-absorbing and heat-emitting ends switch when the current is reversed, which means that the thermoelectric appliance functions as either a heater or a cooler. The following formulas can be used to calculate the thermoelectric cooler's cooling power and electrical power in transient moment, and the ratio of Q_C to P can be used to calculate the TEC coefficient of performance (COP):

$$Q_C = \alpha I T_C - 0.5 I^2 R - K(T_h - T_C), \quad (1)$$

$$P = I^2 R + \alpha I(T_h - T_C), \quad (2)$$

$$\text{COP} = \frac{Q_C}{P}. \quad (3)$$

In the equation, T_h and T_C represent the temperature of the thermoelectric element hot and cold ends, respectively, while R and K stand for the electric resistance and thermal conductivity between the thermoelectric element's hot and cold ends. According to the research of Chen and Snyder [19], the following formulas can be used to calculate α , R , and K . In the following equation, Q_{\max} , T_h , ΔT_{\max} , and I_{\max} are the physical characteristics of the thermoelectric element, which are assumed to be invariant with temperature. Because the hot end temperature T_h is the variable, the R , α and K value of TEC is constantly changing. Generally, the thermoelectric cooler supplier will provide Q_{\max} , ΔT_{\max} , I_{\max} , and V_{\max} values at two different hot end temperatures. According to the formula, two groups of Q_{\max} , ΔT_{\max} , I_{\max} , and V_{\max} values can be calculated. Assuming that these values change linearly with temperature, the R , α and K value

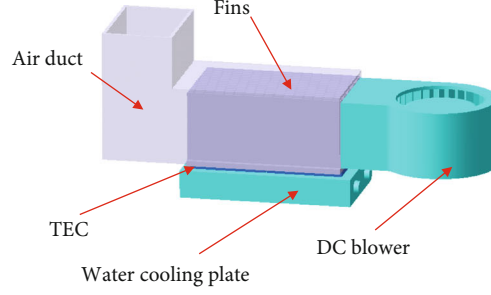


FIGURE 1: Diagram of the TEC assembly.

of the thermoelectric cooler at a certain temperature can be obtained.

$$\alpha = \frac{Q_{\max}(T_h - \Delta T_{\max})}{T_h^2 I_{\max}}, \quad (4)$$

$$R = \frac{N^2 l}{Af} 4\rho, \quad (5)$$

$$K = \frac{Q_{\max}(T_h - \Delta T_{\max})^2}{T_h^2 \Delta T_{\max}}. \quad (6)$$

2.2. Thermoelectric Cooler Geometry. Figure 1 depicts the TEC's geometric model. The TEC makes use of a for-sale TE module (TEC-12706), and the performance parameters are displayed in Table 1. However, when $\Delta T = \Delta T_{\max}$, the $Q_c = 0$, and when $Q_c = Q_{c \max}$, the $\Delta T = 0$, so the maximum temperature difference and the maximum cooling power cannot be realized in practice. The module is 40*40*3.8 mm in size. The thermoelectric module's hot end is fastened to the water-cooled plate. The cold end is connected to the finned radiator, while the hot end heats the water-cooled plate shell, in which the water flow removes the heat; on the other side, the cold end absorbs the heat from the finned radiator. The TEC performs the function of air conditioner because the temperature of the fins drops, so when the air-flow reaches the fins, the temperature will also drop. The DC fan can change the airflow speed over the fins in the range of 0-10 m/s. The TEC-cooled gas travels to the climate-controlled seat's internal air tunnels, which in turn ventilate and cool the occupant's back and buttocks.

2.3. Results and Discussion. The experiment was conducted at an ambient temperature of 25°C. In Figure 2, the associated cooling power Q_c and cooling efficiency COP_c were calculated, and the TEC cold end temperature T_c and the energized current I were monitored. In Figure 2(a), it is discovered that as the current increases, the cold junction's temperature falls, and the time it takes to achieve the stable temperature gradually increases. Furthermore, the bulk of the finned heat sink is significantly more than that of the thermoelectric element, which increases the thermal inertia overall. The equivalent response time increases with increasing temperature difference. However, the T_c rebounds when the current exceeds 5 A, and the reason is that the Joule heat generated inside the TEC exceed the cold end's cooling

TABLE 1: TEC-12706 performance parameter table.

| Specification | T_h | I_{\max} | U_{\max} | ΔT_{\max} | $Q_{c \max}$ |
|---------------|-------|------------|------------|-------------------|--------------|
| TEC-12706 | 27°C | 6.0 A | 15.4 V | 67°C | 55 W |
| | 50°C | 6.0 A | 16.9 V | 71°C | 56 W |

capacity, the current is too large and the temperature difference between the hot and cold ends cannot be too large. As observed in Figure 2(b), the cooling power increases with an increase with current, and the maximum cooling power can reach 19.8 W. However, the increase rate of stable cooling power gradually decreases because of Joule heat. In Figure 2(c), the COP_c decreases as the current I increases, and the decreasing range also gradually reduces. As seen in Figure 2(d), the range of the ideal working current is 3-4 A when the cold-end temperature is obtained between -7.1 to -0.4°C, and the temperature range of the air outlet is 19 to 20°C. Within the appropriate range, the COP value is 0.5-0.7, and the cooling power of the monolithic thermoelectric element is 15-17 W. This is in accordance with the stable results of Q_c , T_c , COP_c , and the air blowing temperature required by the human body [20]. However, T_h really represents the temperature of the cold and hot surfaces of the P-N junction of TEC, but we can only measure the temperature of the ceramic chips on the cold and hot surfaces. However, the ceramic is composed of 96% aluminum oxide, and the thermal conductivity is 20 W/mK, and the thickness is 0.76 mm, the difference between the measured temperature value and T_h is not more than 1°C. Therefore, the measured cold and hot end ceramic sheet temperatures are considered as T_h and T_c . But, the fact that the temperature difference between the hot and cold ends measured in the experiment is smaller than the actual value, which makes the calculated COP and Q_c values slightly larger than the actual values, should be considered.

2.4. Model of the Passenger Car Climate Control Seat. The climate-controlled seat dissipates heat and water vapor produced by the human body through the airflow from the seat, creating a local "microclimate" between the body and the seat. This results in low energy consumption and significantly enhances the thermal comfort of the human body. The seat includes a ventilation layer, a porous medium layer, and a layer of breathable fabric, as shown in Figure 3(a). The climate-controlled seat ventilation layer is where the chilly

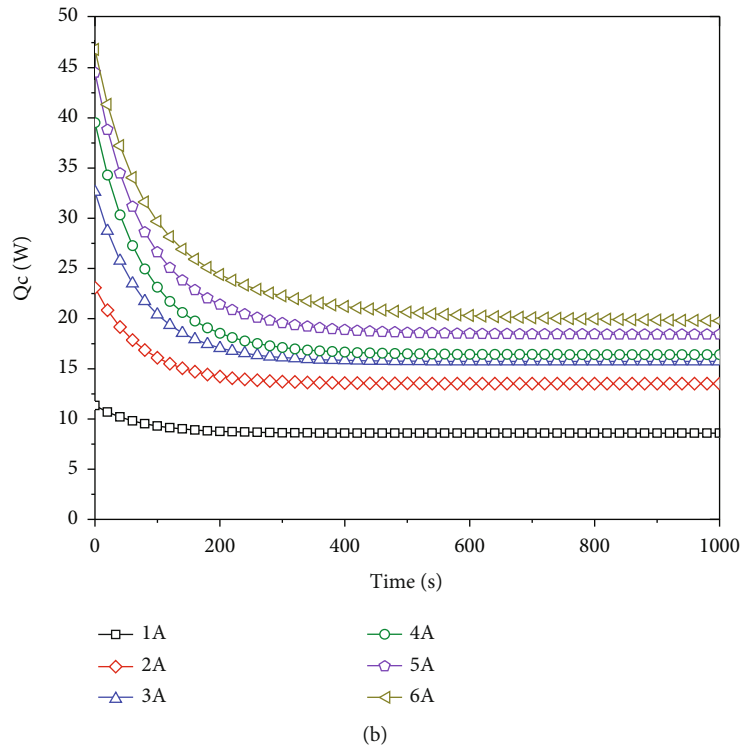
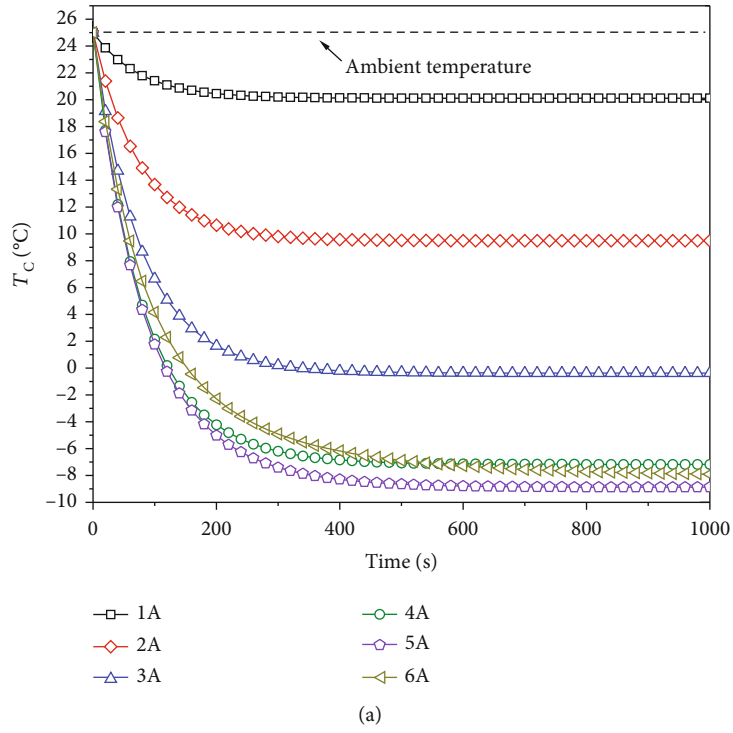


FIGURE 2: Continued.

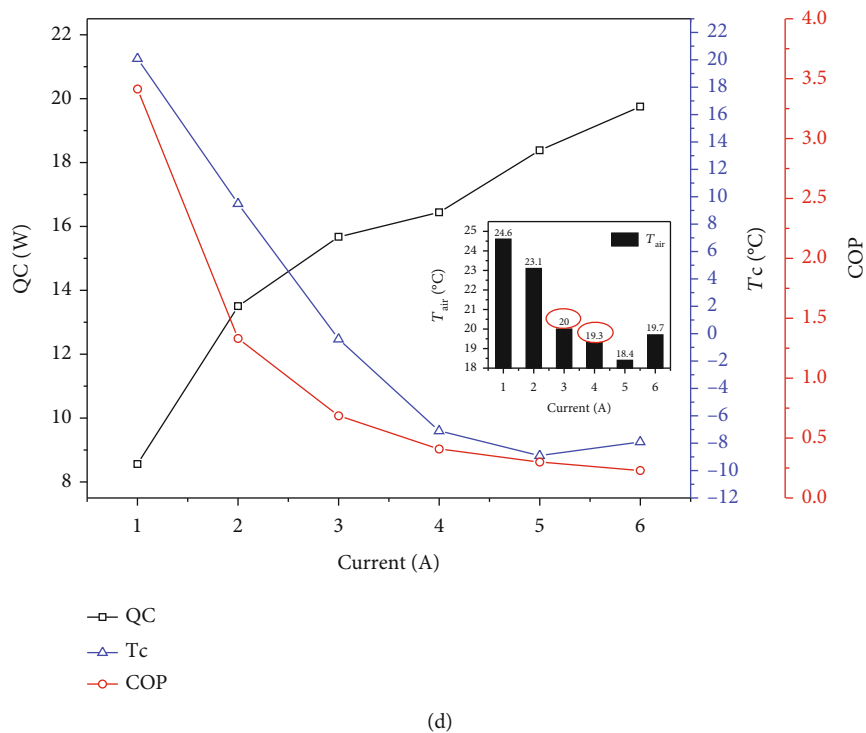
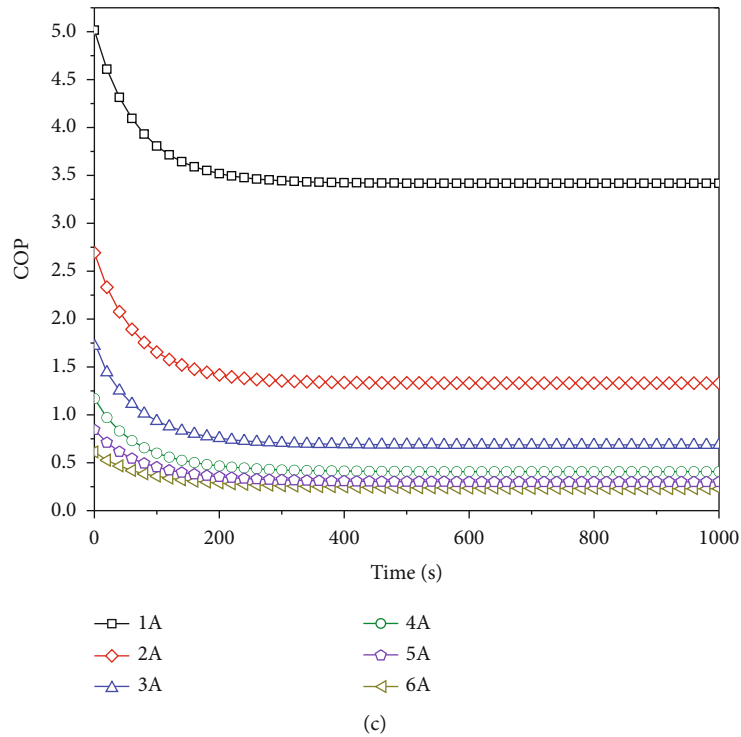


FIGURE 2: The TEC cooling performance: (a) the cold end temperature’s variation with current, (b) cooling power Q_C variation with current, (c) cooling efficiency COP_C variation with current, and (d) diagram depicting the steady-state analysis of Q_C , T_C , and COP_C .

air from the air conditioner enters. The human body’s thighs and back are blasted with the breathable cloth layer. The ventilation layer’s design mimics how the veins in a leaf’s stem are distributed. As seen in Figure 3(b), the leaves may totally rely on their unique stem vein structure to transport moisture from the trunk to all of the leaf’s corners.

2.5. Analysis of Air Distribution Characteristics of Climate-Controlled Seats. Figure 4(a) displays the air velocity distribution over the surface of the backrest and seat cushion for a single occupant in a climate-controlled seat. The velocity distribution is comparatively uniform in the vicinity of the human body. The uniformity is worse than the seat

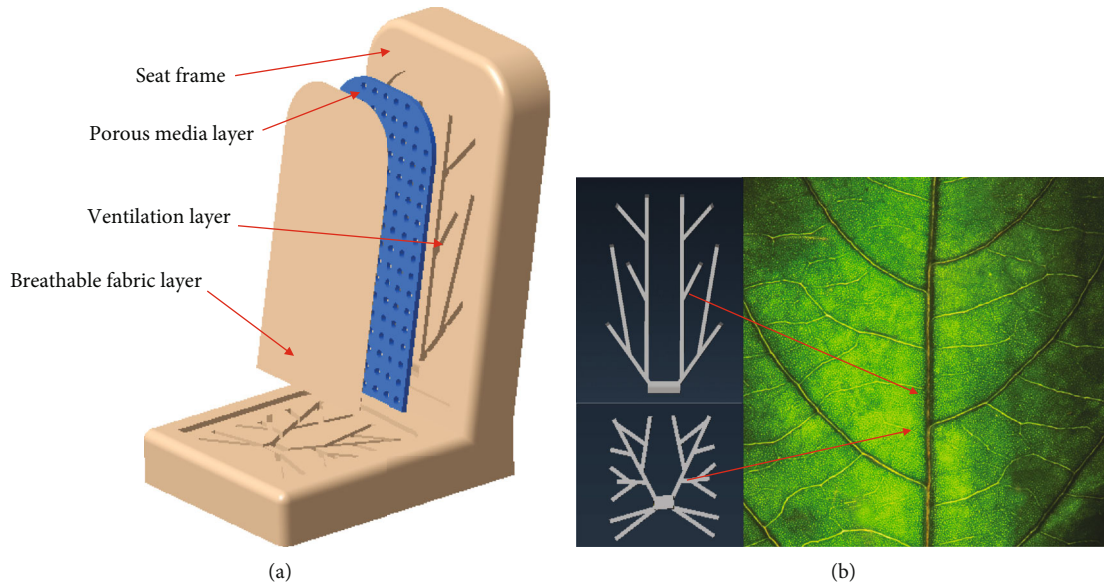


FIGURE 3: The schematic of the climate-controlled seat (a) schematic of climate-control seat structure (b) map of the veins on a leaf stem.

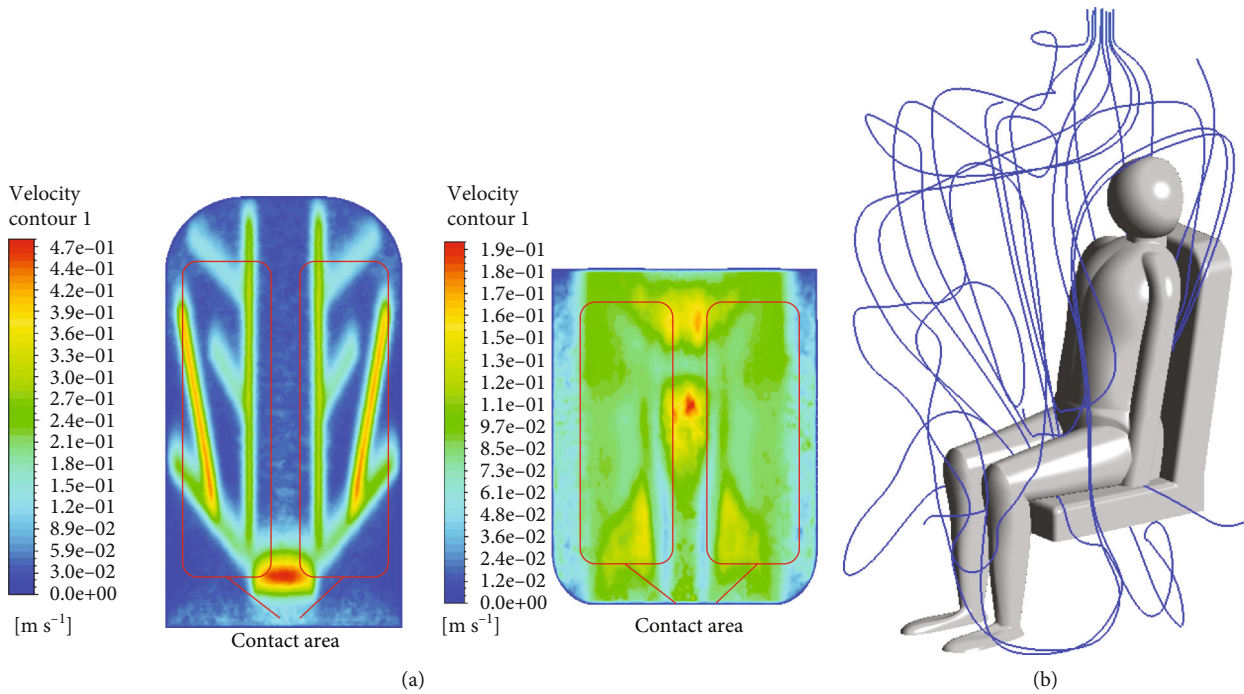


FIGURE 4: The air distribution of the climate-controlled seat (a) contour of air velocity distribution on the surface of the backrest cushion (b) streamline diagram of airflow distribution in the space around the occupant.

cushion’s uniformity. The backrest’s contact area experiences an average airflow velocity of 0.23 m/s, while the seat cushion’s contact area experiences an average airflow velocity of 0.17 m/s. The airflow speed in the contact area is 110% higher and 82.8% faster than that in the surrounding area, respectively. The climate-controlled seat provides a powerful wind blowing sensation while expelling the moisture and heat produced by the human body, which satisfies the body’s need of thermal comfort.

It shows that the velocity streamline around the body of the occupant in Figure 4(b). The velocity streamline is visible

to wrap around the mannequin’s back and buttocks in the figure, and there is a fairly noticeable air flow between the occupant and the seat. It flows to the head, hands, and calves to dispel heat after being blocked by the back and hips.

3. Simulation of the Internal Heat-Flow Field

3.1. Control Equation. The flow of fluid satisfies the law of conservation of mass, momentum and energy, and the air velocity in the vehicle is relatively small, so the air density is basically unchanged, which can be regarded as three-

dimensional incompressible fluid, therefore the $\partial\rho/\partial t = 0$. The equation shows as below.

$$\frac{\partial\rho}{\partial x_i} = 0, \quad (7)$$

$$\rho \frac{\partial u_i}{\partial t} + \rho \frac{\partial u_i u_j}{\partial x_j} = -\frac{\partial p}{\partial x_i} + \frac{\partial}{\partial x_j} \left[\mu \left(\frac{\partial u_i}{\partial x_j} + \frac{\partial u_j}{\partial x_i} \right) \right], \quad (8)$$

$$\rho \frac{\partial T}{\partial t} + \rho \frac{\partial T u_j}{\partial x_j} = \frac{\partial}{\partial x_j} \left(K \frac{\partial T}{\partial x_j} \right). \quad (9)$$

ρ represents air flow density, and μ represents dynamic viscosity. The p represents pressure, and the T is temperature. x indicates the coordinate and the i and j represent coordinate component. The c_p is the specific heat capacity at constant pressure and K is the heat transfer coefficient. To simplify the simulation, the following assumptions are made.

- (1) The sealing between the bulkhead surfaces of the cabin is intact without air leakage. And the radiation heat transfer between the aluminum foil box and other walls is ignored
- (2) The influence of electric wire, communication wire, anemometer, and sensor probe on the surface of aluminum foil box is ignored. And the influence of telescopic rod and sensor on velocity measurement is ignored
- (3) The influence of sensor heating on the temperature field in the experimental cabin is ignored. And the external ambient temperature and air inlet temperature of the default test chamber assumes unchanged

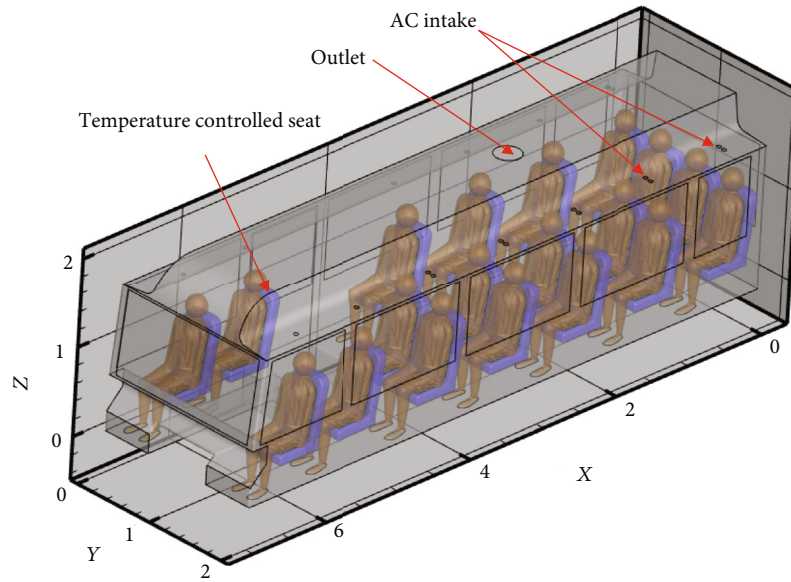
3.2. Internal Heat-Flow Field Simulation Model. The passenger compartment model is depicted in a 1:1 scale in accordance with the Toyota Coaster model, as seen in Figure 5(a). The automobile measures 7000*2000*2000 mm overall. There is one air conditioner inlet above each passenger, and there is an air outlet in the middle of the top of the bus. To simplify the calculation, accessories like the steering wheel, seat belt, and illumination are removed. The passengers were set for 95% manikin, and the body surface temperature is set to 36.4°C, and the heating power of a single passenger is set to 57 W according to the reference [15]. All seats were installed ventilation system to assure the comfort of each passenger. For ease of display, the passengers are numbered by column, as seen in Figure 5(b). Because the calculation domain involves the mutual coupling of climate-controlled ventilation duct, porous medium, and cabin air, the calculation model adopts tetrahedral unstructured grid with mesh sizes of 2 mm at the inlets and outlet, 3 mm at the human body and climate-controlled seats, and 3 mm at the windows and front windshield is chosen since it is more complicated. Finally, the overall mesh of the computation model is produced, which is 5 mm. As revealed by

the grid independence verification in Figure 5(c), the grid should have a minimum population of 10.5 million.

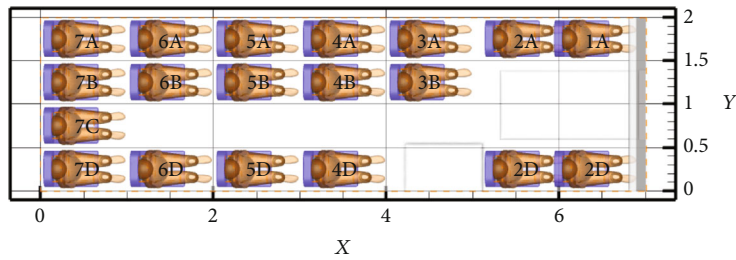
3.3. Numerical Calculation Methods and Boundary Conditions. Sunlight is more intense during the summer, and solar radiation is one of the key factors contributing to the rise of temperature. During the calculation, both the DO radiation model and solar trace are activated. Consider the Chinese city of Wuhan, which is situated at 114° east longitude and 30° north latitude. The time is set at 14:00 PM on July 16 in the East 8 time zone. The airflow that affects the human body originates from the buttocks, the back of the climate-controlled seat, and the air inlet of the air conditioner. It is possible to think of the interplay of different airflows as an incompressible turbulent flow. According to the equation $Re = \rho v d / \eta$, the Reynolds number is 23600, so the realizable k- ϵ model [21] is used in the turbulence model. The momentum, turbulent kinetic energy, turbulent dissipation rate, and energy space discrete algorithms are all set to the first-order upwind style, while the pressure and velocity coupling algorithm is set to SIMPLE. According to the equation $Q_C = c_1 m_1 (T_1 - T_3) + c_2 m_2 (T_2 - T_3) + Q_A$, The air conditioning cooling load power is about 10400 W, and there are 38 TECs in the cabin which cooling load power is about 500 W. The inlet temperature is set to 16°C, the air conditioner's speed intake is set to speed inlet, the wind speed is set to 5 m/s, and the outlet is set to pressure outlet. The ventilation air duct within the climate-controlled seat back and cushion is also set as velocity inlet. The passenger compartment's interior and exterior walls, the instrument panel, and the floor all experience heat transfer processes while the outset air temperature is set at 30°C. These processes include conduction, radiation, and heat radiation. Mixed boundary conditions are used, and Table 2 below lists the physical characteristics of each wall surface:

3.4. Validation of Simulation Methods. An experimental cabin with an air vent in the middle was constructed to test the simulation's accuracy. This cabin is depicted in Figure 6(a). And Figure 6(b) depicts the location and dimensions of the air inlet and outlet. The maximum air volume of the fan in the experimental chamber is 1800 m³/h, and one side of the cabin is built of acrylic plate in convenient for observation. The static pressure box distributes the airflow uniformly to each air intake through the air supply duct, and the airflow travels through the inner wall and the seat before exiting from the return air outlet thanks to the adjustable fan.

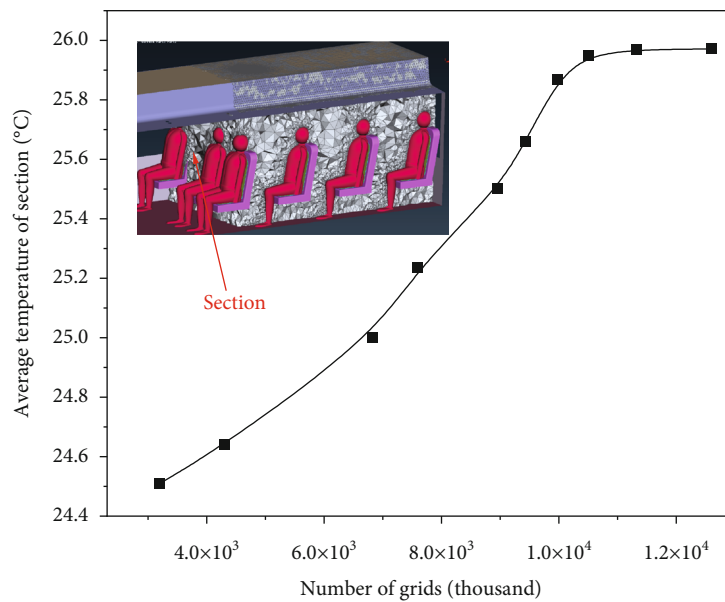
The experimental cabin adopts an equal scale model, with each air inlet's recorded wind speed used to be the simulated inlet condition. TSI-9594 hot wire anemometer is used for wind speed measurement, with resolution of 0.01 m/s and accuracy of $\pm 3\%$. The industrial temperature sensor is used for temperature measurement, and the measurement accuracy is $\pm 0.4^\circ\text{C}$. Three different positions of the middle area of the experimental cabin were measured, as seen in Figure 6(b), and each position has six points. The wind speed of these points was measured, and then



(a)



(b)

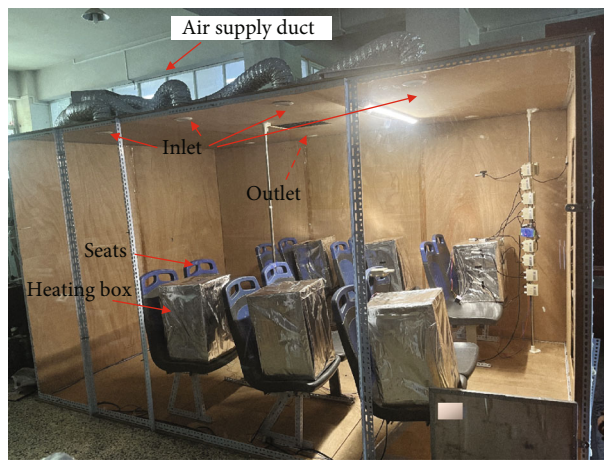


(c)

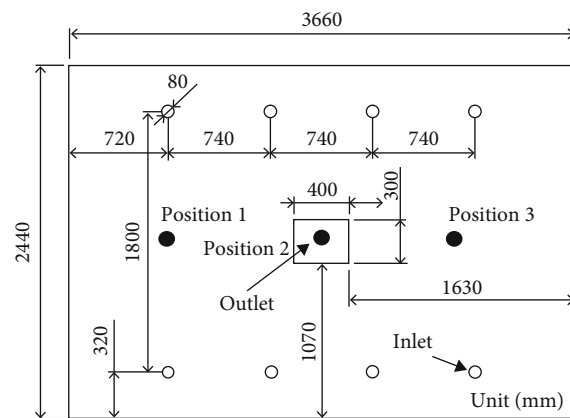
FIGURE 5: The diagram of the passenger compartment and grid independent verification. (a) Schematic diagram of the passenger compartment model with climate-controlled seats. (b) Crew number diagram. (c) Grid independence verification.

TABLE 2: Physical parameter table of each part.

| Parts | Front windshield | Window glass | Car shell | Floor | Dashboard | Seat | Passenger |
|--|------------------|----------------|---------------------|---------------------|-----------|---------|-----------|
| Thickness (mm) | 5 | 3.5 | 8.6 | 7.6 | 12 | 5 | 10 |
| Material | Laminated glass | Tempered glass | Multilayer material | Multilayer material | Plastic | Leather | — |
| Density ($\text{kg}\cdot\text{m}^{-3}$) | 2529.5 | 2529.5 | 8031 | 930 | 1200 | 481 | 1100 |
| Thermal conductivity ($\text{W}\cdot\text{m}^{-1}\cdot\text{K}^{-1}$) | 0.92 | 0.73 | 7.65 | 0.93 | 2.7 | 0.135 | 0.432 |
| Heat capacity ($\text{J}\cdot\text{kg}^{-1}\cdot\text{K}^{-1}$) | 754 | 790 | 502.48 | 1480 | 1502 | 860 | 4200 |
| Heat transfer coefficient ($\text{W}\cdot\text{m}^{-2}\cdot\text{K}^{-1}$) | 6.38 | 4.6 | 28.8 | 4.68 | 10 | 15 | 20 |
| Absorption rate | 0.4 | 0.4 | 0.58 | 0.58 | 0.82 | 0.58 | 0.8 |
| Emissivity | 0.1 | 0.1 | 0.42 | 0.42 | 0.19 | 0.42 | 0.2 |
| Transmittance | 0.5 | 0.5 | 0 | 0 | 0 | 0 | 0 |



(a)



(b)

FIGURE 6: The cabin diagram and dimension drawing. (a) Experimental cabin diagram. (b) Dimension drawing of the top of the laboratory cabin.

compared with the simulation results. According to experimental and simulation data, as depicted in Figure 7, the air velocity is the greatest at the midway height of the position 1 and position 3, which is 0.2 m/s and 0.4 m/s, respectively. While the maximum airflow speed at the position 2 appears at the highest point, at around 0.45 m/s, because the airflow from the air inlet meets the box and seat, and then generates backflow, preventing most of the airflow from reaching the bottom. The comparison from simulation and experiment shows that the highest point is closest to the air outlet. Due to the box and seat's blocking effect as well as the superposition of the air inlet velocity measurement and the wind velocity measurement error at each point, the airflow velocity at position 2 middle position also has an extreme value. Even though there is some divergence and the average inaccuracy is roughly 32%, which was caused by the superposition of air inlet wind speed and measuring point wind speed's measurement error, blocking of the support rod and air leakage of the cabin. The overall trend of the simulation and the maximum wind speed point are the same, demonstrating the validity of the simulation approach. In order to reduce the bias, the cabin should be made more sealed

or a more accurate wind speed measurement method such as Particle Image Velocimetry (PIV) should be applied.

As showed in Figure 8, there is one light bulb in each box, and the working state of the light bulb was decided by the thermocouple pasted on the surface of the box. The heated box surface upper and lower limits temperature was set to 44-46°C, and nine temperature sensors were used to measure the temperature near the box and experiment cabin wall. The inlet temperature as seen in the figure is set as 31°C, and the velocity is set as 8 m/s. Point 1 and point 2 are away from the heated box, and other seven points are near the box. Although the experimental and simulation data of points 1 and 2 are quite different which may be caused by boundary condition settings, the simulation data of other points are within the error range of the experimental data. The above shows that the temperature field simulation is reliable.

4. Results of Simulations and Analyses

Fourteen different body parts, including the head, chest, back, and legs, had their comparable temperatures measured

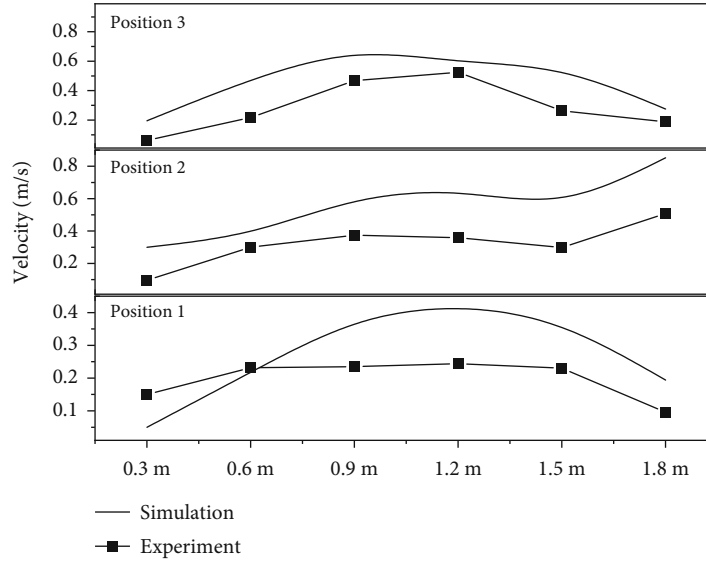


FIGURE 7: Wind velocity comparisons between experiment and simulation at various points.

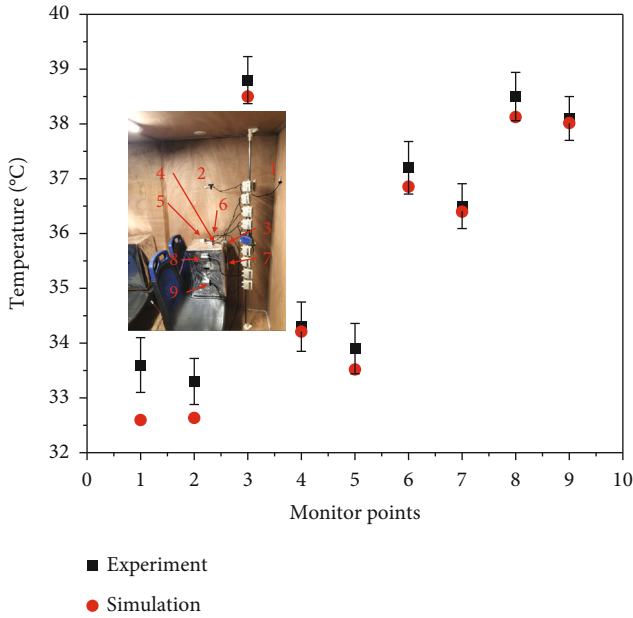


FIGURE 8: Temperature comparisons between experiment and simulation around the heated box.

in order to make it easier to analyze how the climate-controlled seat improved the thermal comfort of the passengers. Consider the ideal “cold head and hot feet” scenario when evaluating the thermal comfort of the human body.

4.1. Analysis of the Heat-Flow Field in the Cabin. In order to discuss the effect of increasing the thermal comfort of passenger car occupants after installing climate-controlled seats, the simulation cases given in Table 3 are designed.

Figure 9 displays the temperature contour of several components on the bus’s interior surface when it is exposed to the sun. The window glass can reach temperatures of about 37°C due to solar radiation and heat absorption capacity of the glass, whereas other maintenance structures can

TABLE 3: Working case setting scheme.

| Case | AC | Climate-control seat |
|-------|-------|----------------------|
| Case1 | Open | Open |
| Case2 | Open | Close |
| Case3 | Close | Open |
| Case4 | Close | Close |

only reach temperatures of 29 to 30°C. The reason for the above phenomenon is that the way glass gets heat is mainly solar radiation, while the way other walls to get heat is mainly heat conduction. Not surprisingly, the inner surface temperature of the air-conditioning duct, which is located inside the passenger car’s upper casing and is not in contact with ambient air outside and not affected by solar radiation, so the surface temperature is only 16°C.

Figure 10 display the temperature and velocity contour for section 1 of the passenger cabin for case1, 2, and 3. In operating case 1, the traditional air conditioners and climate-controlled seats are both open, resulting in the average cabin temperature of 23.45°C. In case 3, only the climate-controlled seats cool the passengers, resulting in low temperatures in the occupants’ backs and buttocks, but high temperatures in other frontal areas, which results in poor occupants’ thermal comfort. The traditional air conditioner is turned on in both operating scenarios, as indicated in Figures 10(d) and 10(e), and the air flow from the traditional air conditioner blows to the occupant’s face, chest, and thighs. However, the addition of seats increases the turbulence around the passengers, enhancing the heat transfer between the passengers and the environment. Therefore, the climate control seat in Case 1 increases the return flow of typical air conditioning airflow after striking the passenger’s body and seat, thus improving the overall thermal comfort of the passenger. It can be seen that the use of climate-controlled seats makes up for the shortcomings of traditional bus air

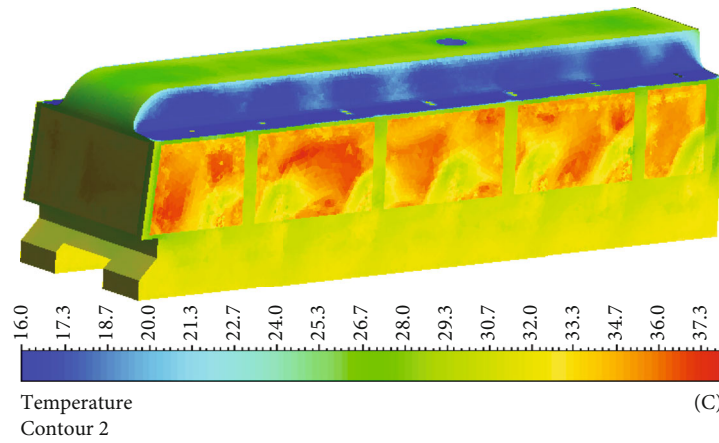


FIGURE 9: Contour showing passenger cabin surface temperature dispersion.

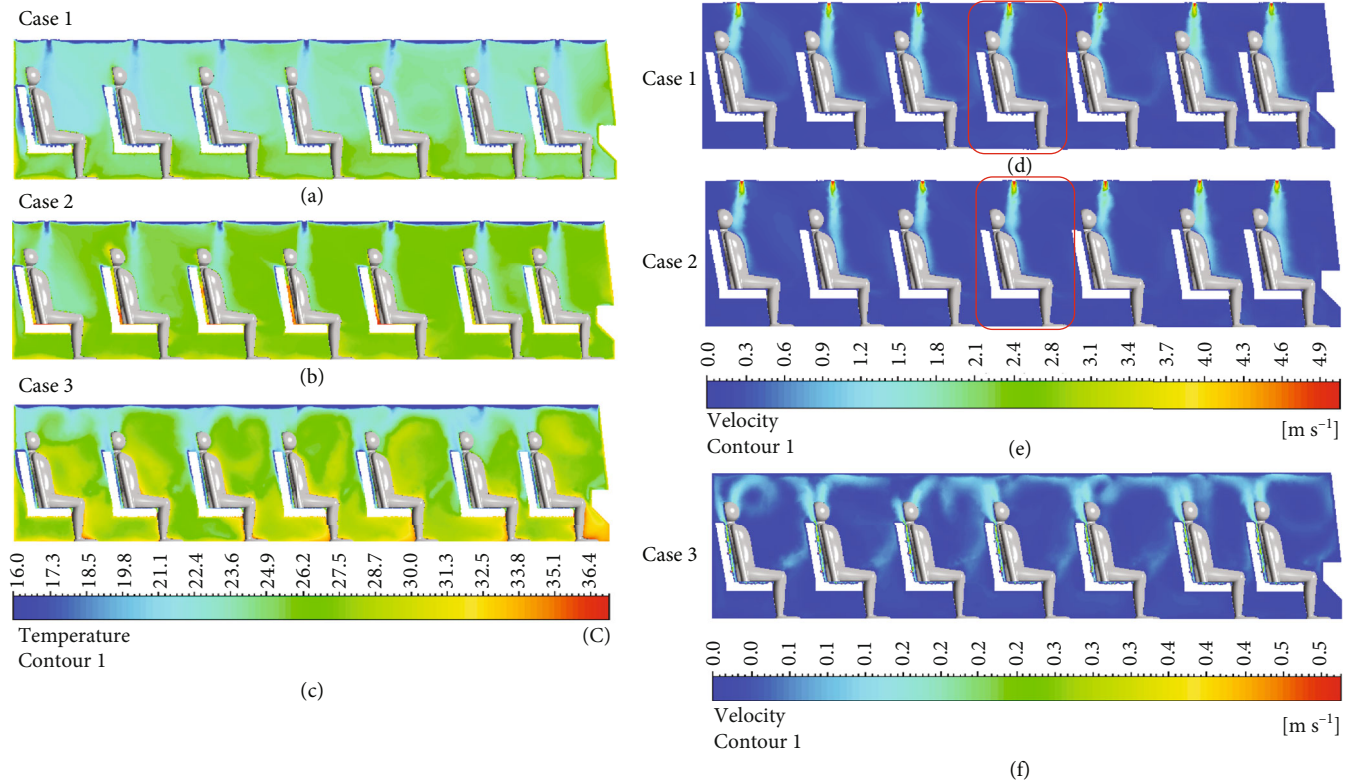


FIGURE 10: Contour showing the temperature and velocity dispersion in section 1 of the passenger cabin.

conditioners. As shown in Figure 10(f), the air flow from the climate-controlled seat blows toward the back and buttocks of the human body before dissipating from the head and thighs, removing the water vapor and heat produced by the human body, in other words, the role of seats in improving thermal comfort should not be underestimated.

The temperature distribution of the human body’s front surface of the occupant under case 1 is depicted in Figure 11. Although the upper body of Row A passengers is exposed to the sun, the air temperature near the head, chest, and arms is lower for passengers in rows A and D than those in rows B and C, since passengers in rows A and D are seated closer

to the air inlets of the air conditioner. According to the thermal comfort theory of “cold head and warm feet”, the temperature above the occupant’s chest is lower than the temperature in the leg area, which means the passengers are in thermal comfortable state.

4.2. *Thermal Comfort Evaluation.* According to technical standards [22], the climate-controlled seat could create a comfortable local thermal environment for passengers. The evaluation indicators are equivalent temperature (T_{eq}) and overall thermal comfort deviation (A_{EQT}). The equivalent temperature indicates that this area of the human body is

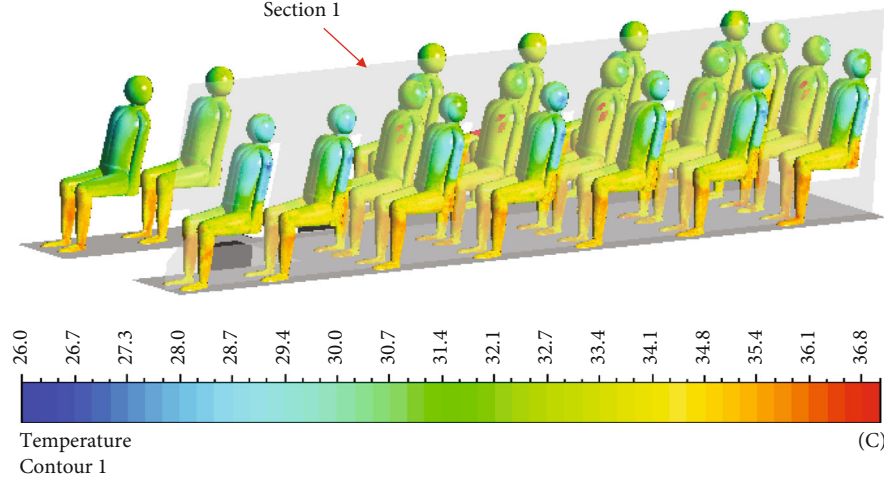


FIGURE 11: Graph of the frontal body temperature of the person in a working state's temperature.

at a comfortable temperature. The more closely the equivalent temperature approaches the midpoint of the comfort range, the more comfortable it is. The range of the overall thermal comfort deviance is -1 to 1. A temperature in the range of 0 to 1 is considered to be comfortable. The value increases in comfort as it increases in size. If the value is between -1 and 0, the analogous temperature is said to be in the uncomfortable range. The following is the comfort deviation equation:

$$T_{eq,i} = T_{s,i} - \frac{8.3v_{air,i}^{0.6} \cdot S_i \cdot (T_{s,i} - T_{a,i})}{h_{cal,i} \cdot S_i} + \frac{\sum_n \sigma \cdot \epsilon_i \cdot f_{i,n} \cdot (T_{s,i}^4 - T_n^4) + Q_{sol}}{h_{cal,i} \cdot S_i}, \quad (10)$$

$$A_{EQT} = \sum \omega_i A_i, \quad (11)$$

$$A_i = \frac{1/2(T_{max,i} - T_{min,i}) - |T_{eq,i} - 1/2(T_{max,i} + T_{min,i})|}{1/2(T_{max,i} - T_{min,i}) + |T_{eq,i} - 1/2(T_{max,i} + T_{min,i})|} \times 100\%. \quad (12)$$

In the equation, $T_{eq,i}$ is the equivalent temperature of the i -section of the human body; $T_{s,i}$ is the skin surface temperature of the i -section of the human body; $v_{air,i}$ is the air velocity near the i -section of the human body. A_{EQT} is calculated by the thermal comfort weight of each part of the human body, so it represents the overall thermal comfort deviation and it indicates the deviation degree between the overall thermal comfort of human body and its ideal comfortable temperature. ω_i represents the weight of the thermal sensation of the body part on the overall thermal sensitivity, as shown in Table 4 [23], A_i is the local thermal comfort deviation of the i -th part of the human body. T_{max} and T_{min} are the upper and lower limits of the comfort equivalent temperature of the section of the human body.

TABLE 4: Table of the weighting factors for different body parts' thermal sensations.

| Parts | Weights |
|------------|---------|
| Head | 0.16 |
| Chest | 0.18 |
| Back | 0.18 |
| Upper arms | 0.07 |
| Lower arm | 0.07 |
| Hands | 0.08 |
| Thigh | 0.07 |
| Calf | 0.08 |
| Feet | 0.11 |

For the occupants who are close to the front and rear windows, the center window, and those who are not near the window, the corresponding temperature of each area of the body and the deviation of the total thermal comfort are examined. Figure 12 illustrates the blue colored area as the body's thermal comfort zone. When equivalent temperature is closer to the midpoint, the more comfortable the passenger feels. The equivalent temperature under the legs of all occupants in the four working scenarios is much higher than the comfort zone, because the body's legs and feet are located far from the inlet of the air conditioner, making it difficult for the cold air to reach. However, Table 4 reveals that the region below the legs has little impact on the overall thermal comfort of the passenger because the thermal sensation weighting factor only accounts for 1/5 of all.

In case 1, the occupants' overall thermal comfort is at the highest level. And in case 2, less airflow passes through the occupant's back and buttocks, and the local equivalent temperature is higher than the comfort zone, which lowers the occupant's overall thermal comfort. Case 3 has the equivalent temperature of the occupant's back and buttocks dropped to a comfortable level, while other body parts equivalent temperatures are much higher. Case 4 has no air conditioning, and the equivalent temperature is as high as 36°C, with the worst thermal comfort. The results indicate

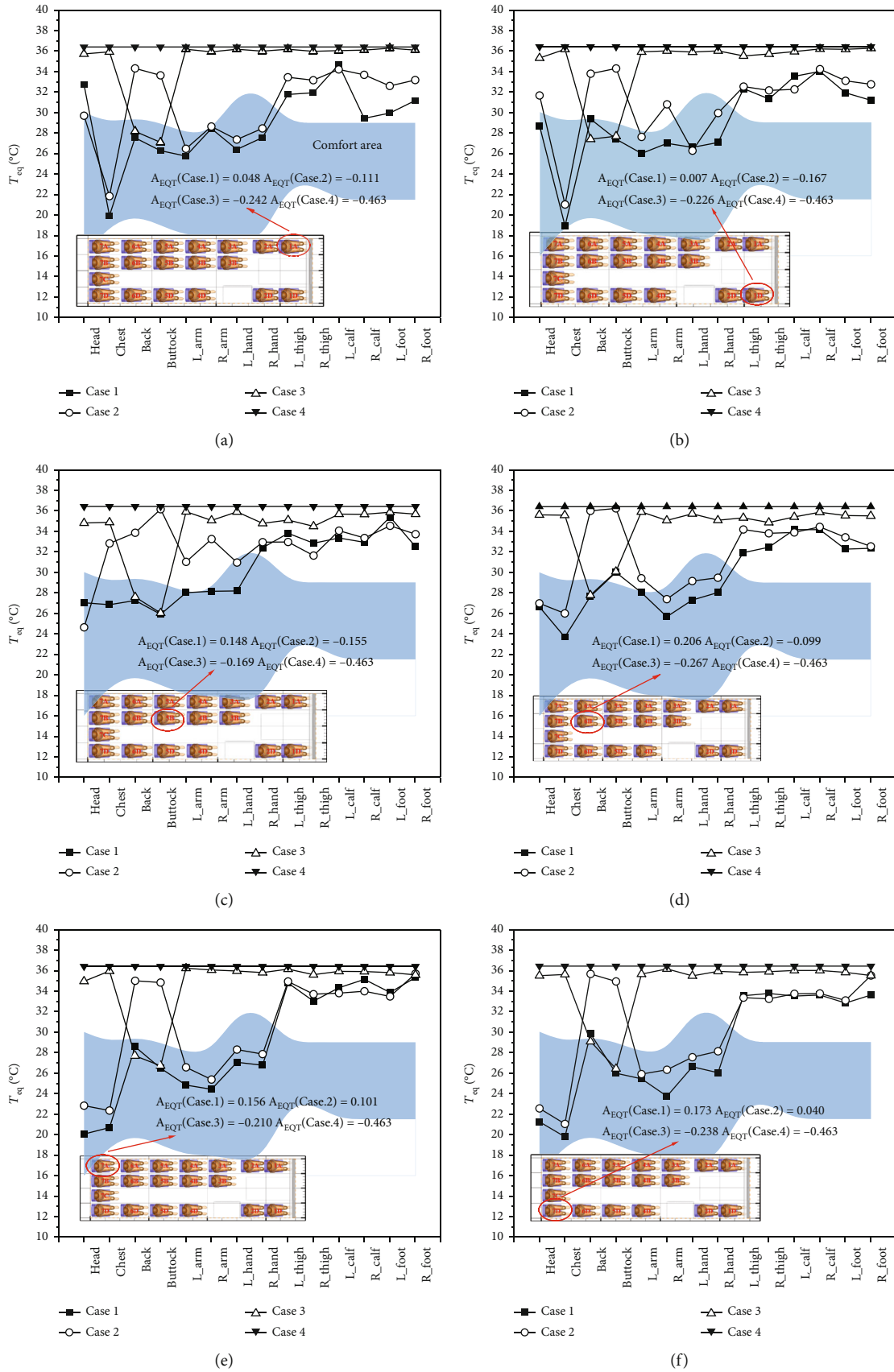


FIGURE 12: Equivalent temperature distribution map of occupant body.

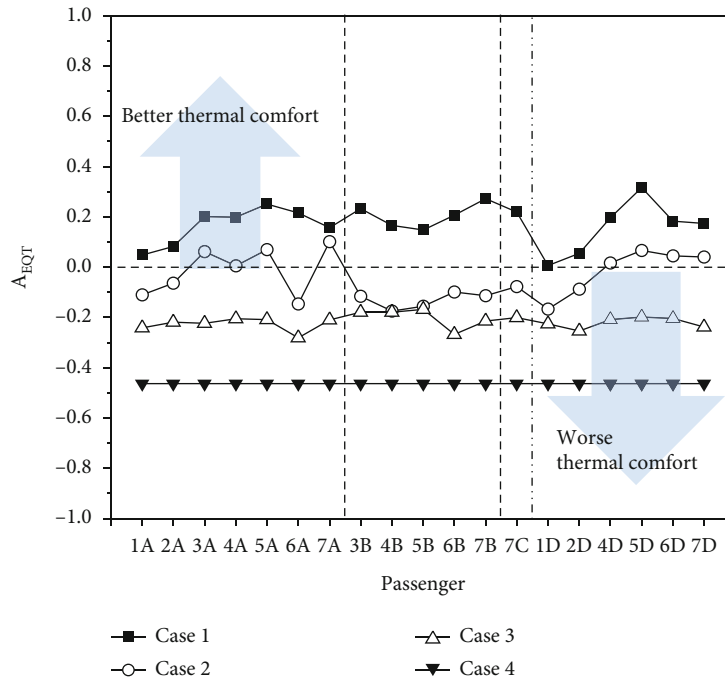


FIGURE 13: Occupant's overall thermal perception deviation.

that the thermoelectric cooling climate-controlled seat is an effective way of delivering cooling air and increasing thermal comfort, which is consistent with the research results of Su et al. [15].

First of all, in case 1 (under the simultaneous influence of traditional air conditioning and climate-controlled seats), the thermal comfort weighting factors head and chest thermal comfort reflect the overall thermal comfort deviation of passengers. The equivalent temperature of front window passengers 1A and 1D is highest, the equivalent temperature of middle window passengers is moderate, and the equivalent temperature of rear window passengers 7A and 7D is lowest. The reason is that the front row passengers can receive solar radiation at the front and side, and there are only two air conditioner providing cold air for front row passengers. Although the passengers in the rear row are also exposed to a certain amount of solar radiation, there are four air conditioning inlets above, which could provide sufficient cold airflow. So, in order to meet the thermal comfort of every passenger, the temperature of some air inlets should be lower or the wind speed should be higher. The thermal comfort deviation of B5 and B6 passengers without windows in the middle is 0.148 and 0.206, which is better than that of front and rear row passengers. The above analysis is based on constant thermoelectric cooling power. Under case 1, although the thermal comfort of some passengers is not well met due to various reasons, the problem can be solved by personalized control of TEC cooling power [24].

The overall thermal comfort variation of 19 passengers under 4 working cases is displayed in Figure 13. In case 1, all of the occupants are generally comfortable and the occupant thermal feeling deviation A_{EQT} is between 0.1 and 0.3. In case 2, A_{EQT} of eight occupants is above zero which means

they are thermally comfortable, and the overall thermal sensory deviation is generally comfortable. In case 3 and 4, the passengers are all in a moderately unpleasant state, with rows B and C having the largest thermal sensory variances, respectively, between -0.2 and -0.1. Since the traditional air conditioner does not provide adequate cooling and is located far from the air inlet, where the equivalent temperature of the head and chest is higher than that of the passenger by the window, the overall thermal sensory deviation of the passengers in working cases 3 and 4 exhibits a poor level.

5. Conclusion

In order to research and analyze the thermal comfort of the human body in the passenger compartment of the passenger automobile under four operating circumstances, the findings are as follows:

- (1) The climate-controlled seat TEC's ideal operating current range is 3–4 A, its cold end temperature is 19–20°C, and its single-chip thermoelectric element has a cooling capacity of 15–17 W
- (2) In case 2, the best and worst thermal comfort deviations are 0.101 and -0.167. Passengers closer to windows enjoy more thermal comfort than those who do not. The thermal comfort of the occupant's back, the region between the buttocks and the seat, and the overall thermal sensation of all occupants can be improved to a more pleasant level after installing the climate-controlled seat system (case 1). Compared to working case 2, the overall thermal comfort of the 19 passengers has increased by 18.96% in case 1

- (3) The overall thermal comfort of the passengers from the front to the rear displays a trend of first rising and then falling, and the overall thermal comfort of the passengers in the middle and rear rows is the best when the traditional air conditioner and climate-controlled seats are turned on simultaneously (case 1). For passengers in the back, the ideal thermal comfort deviation can be as low as 0.316

In order to improve the reliability of simulation and results, the velocity and temperature experiment of real vehicles need to be carried out, and the actual climate-controlled seat need to be made to verify the accuracy of the analysis.

Nomenclature

| | |
|---------------|--|
| $T_{eq,i}$: | Equivalent temperature of the i -section of the human body |
| $T_{s,i}$: | Skin surface temperature of the segment |
| $v_{air,i}$: | Air velocity around the segment |
| $T_{air,i}$: | Air temperature around the segment |
| $f_{i,n}$: | Effective radiation area coefficient of the segment |
| $h_{cal,i}$: | Convection heat transfer coefficient |
| S_i : | Surface area of the segment |
| A_i : | Local thermal comfort of the segment |
| A_{EQT} : | Overall thermal comfort |
| $T_{max,i}$: | Upper limit of the equivalent temperature |
| $T_{min,i}$: | Lower limit of the equivalent temperature |
| Q_C : | Cooling power |
| I : | Current |
| R : | Resistance |
| K : | Thermal conductivity |
| T_h, T_C : | Temperature of hot and cool side |

Greek Symbols

| | |
|-------------------|---|
| α : | Seebeck coefficient |
| σ : | Stefan constant |
| ε_i : | Emissivity |
| ω_i : | Weight coefficient of thermal sensation |

Acronyms

| | |
|-------|--|
| HVAC: | Heating, ventilating, and air conditioning |
| CFD: | Computational fluid dynamics |
| TEC: | Thermoelectric cooler |
| COP: | Coefficient of performance |
| DO: | Discrete ordinates |
| AC: | Air conditioner |

Data Availability

The data that support the findings of this study are available from the corresponding author upon reasonable request.

Conflicts of Interest

The authors declare that they have no conflicts of interest.

Acknowledgments

This work was supported by National Natural Science Foundation of China (Grant No. 51805387).

References

- [1] Q. Wan, C. Su, X. Yuan, L. Tian, Z. Shen, and X. Liu, "Assessment of a truck localized air conditioning system with thermoelectric coolers," *Journal of Electronic Materials*, vol. 48, no. 9, pp. 5453–5463, 2019.
- [2] H. Du, Y. P. Wang, X. H. Yuan, Y. D. Deng, and C. Q. Su, "Experimental investigation of a temperature-controlled car seat powered by an exhaust thermoelectric generator," *Journal of Electronic Materials*, vol. 45, no. 3, pp. 1529–1539, 2016.
- [3] R. Buchalik and G. Nowak, "Technical and economic analysis of a thermoelectric air conditioning system," *Energy and Buildings*, vol. 268, pp. 112–168, 2022.
- [4] D. Liu, F. Zhao, H. Yang, and G. F. Tang, "Thermoelectric mini cooler coupled with micro thermosiphon for CPU cooling system," *Energy*, vol. 83, pp. 29–36, 2015.
- [5] S. B. Riffat and X. Ma, "Thermoelectrics: a review of present and potential applications," *Applied Thermal Engineering*, vol. 23, no. 8, pp. 913–935, 2003.
- [6] R. Ji, T. Pan, G. Peng, J. Ma, N. Yang, and Q. Hao, "An integrated thermoelectric heating-cooling system for air sterilization— a simulation study," *Materials Today Physics*, vol. 19, article 100430, 2021.
- [7] H. Lim, Y. Kang, and J. Jeong, "Thermoelectric radiant cooling panel design: numerical simulation and experimental validation," *Applied Thermal Engineering*, vol. 144, pp. 248–261, 2018.
- [8] M. Cosnier, G. Fraisse, and L. Luo, "Etude experimentale et numerique sur un systeme thermoelectrique de refroidissement et de chauffage d'air," *International Journal of Refrigeration*, vol. 31, no. 6, pp. 1051–1062, 2008.
- [9] X. H. Yuan, C. H. Qin, Y. P. Wang, and X. Liu, "Characteristics analysis of small insulated vans based on thermoelectric cooling," *Frontiers in Energy Research*, vol. 531, p. 9, 2021.
- [10] M. Zhang, Z. Li, Q. Wang, Y. Xu, P. Hu, and X. Zhang, "Performance investigation of a portable liquid cooling garment using thermoelectric cooling," *Applied Thermal Engineering*, vol. 214, article 118830, 2022.
- [11] C. Rosaria, N. Alessandro, and C. Chiara, "Comfort seat design: thermal sensitivity of human back and buttock," *International Journal of Industrial Ergonomics*, vol. 78, article 102961, 2020.
- [12] U. Pala and H. R. Oz, "An investigation of thermal comfort inside a bus during heating period within a climatic chamber," *Applied Ergonomics*, vol. 48, pp. 164–176, 2015.
- [13] S. Yun, C. Chun, J. Kwak et al., "Prediction of thermal comfort of female passengers in a vehicle based on an outdoor experiment," *Energy and Buildings*, vol. 248, article 111161, 2021.
- [14] A. Warey, S. Kaushik, B. Khalighi, M. Cruse, and G. Venkatesan, "Data-driven prediction of vehicle cabin thermal comfort: using machine learning and high-fidelity simulation results," *International Journal of Heat and Mass Transfer*, vol. 148, article 119083, 2020.
- [15] C. Su, W. Dong, Y. Deng, Y. Wang, and X. Liu, "Numerical and experimental investigation on the performance of a

- thermoelectric cooling automotive seat,” *Journal of Electronic Materials*, vol. 47, no. 6, pp. 3218–3229, 2018.
- [16] O. Hatoum, N. Ghaddar, K. Ghali, and N. Ismail, “Experimental and numerical study of back-cooling car-seat system using embedded heat pipes to improve passenger's comfort,” *Energy Conversion and Management*, vol. 144, pp. 123–131, 2017.
- [17] A. Afzal, C. A. Saleel, I. A. Badruddin et al., “Human thermal comfort in passenger vehicles using an organic phase change material- an experimental investigation, neural network modelling, and optimization,” *Building and Environment*, vol. 180, article 107012, 2020.
- [18] T. Gong, Y. Wu, L. Gao, L. Zhang, J. Li, and T. Ming, “Thermo-mechanical analysis on a compact thermoelectric cooler,” *Energy*, vol. 172, pp. 1211–1224, 2019.
- [19] M. Chen and G. J. Snyder, “Analytical and numerical parameter extraction for compact modeling of thermoelectric coolers,” *International Journal of Heat and Mass Transfer*, vol. 60, pp. 689–699, 2013.
- [20] S. K. Sansaniwal, J. Mathur, and S. Mathur, “Review of practices for human thermal comfort in buildings: present and future perspectives,” *International Journal of Ambient Energy*, vol. 43, no. 1, pp. 2097–2123, 2022.
- [21] L. Karthick, D. Prabhu, K. Rameshkumar, T. Prabhu, and C. A. Jagadish, “CFD analysis of rotating diffuser in a SUV vehicle for improving thermal comfort,” *Materials Today: Proceedings*, vol. 52, pp. 1014–1025, 2022.
- [22] Sae, *Equivalent Temperature-Truck and Bus*, Warrendale, 2001.
- [23] H. Zhang, E. Arens, C. Huizenga, and T. Han, “Thermal sensation and comfort models for non-uniform and transient environments, part III: whole-body sensation and comfort,” *Building and Environment*, vol. 45, no. 2, pp. 399–410, 2010.
- [24] J. Maier, O. Zierke, H. Hoermann, and P. Goerke, “Effects of personal control for thermal comfort in long-distance trains,” *Energy and Buildings*, vol. 247, article 111125, 2021.